Stress Analysis of Bacteria Submitted to Extrusion Loading

A Thesis

Presented to the Faculty of the Graduate School

of Cornell University

In Partial Fulfillment of the Requirements for the Degree of

Master of Science

by

Yu-Chern (Chad) Wong

December 2018

ABSTRACT

Bacteria are known to sense and respond to mechanical signals. To examine bacterial mechanics and their relation to biological responses, we used a microfluidic device to apply a mechanical loading condition we refer to as extrusion loading to individual *Escherichia coli*. Extrusion loading was generated by flowing bacteria in liquid media into tapered constrictions. A difference in fluid pressure across the bacteria and the frictional and normal forces from the channel walls generate loads and deformations on the bacteria. The recent experimental findings in our group suggests that extrusion loading can influence growth rates and the performance of cell membrane proteins involved in the resistance to toxins. Mechanical models of bacteria under extrusion loading were developed to determine the stress state and Young's modulus of the cell envelope.

Here I used analytical and finite element models to characterize the stresses in the cell envelope of bacteria submitted to extrusion loading. The analytical model was derived based on a force balance and transversely isotropic constitutive laws. An axisymmetric nonlinear finite element model was developed using solid elements with transversely isotropic material properties. As many aspects of bacteria material properties are not known, a parametric analysis was performed to determine the combinations of material properties that yielded finite element simulations consistent with experimental results. We found that extrusion loading led to increases

in tensile axial stress, shear stress, and compressive radial stress, and decreases in tensile hoop stress. Besides, the internal pressure on bacteria (the "turgor pressure") increased during extrusion loading.

Additionally we used a series of analytical and finite element models to determine the cell envelope Young's modulus. The analytical model provided a closed form solution for Young's modulus. An axisymmetric nonlinear finite element model was developed using solid elements with isotropic material properties to identify the cell envelope Young's moduli that were consistent with experimental observations. The analytical analysis was extremely sensitive to experimental measurements suggesting that small errors in measurement would have large effects on the predicted Young's modulus. The parametric finite element analysis showed resulting deformations insensitive to the tested range of Young's moduli, preventing us from iteratively determining a Young's modulus. Proposed future approaches to determine the cell envelope Young's modulus are discussed.

BIOGRAPHICAL SKETCH

Yu-Chern Wong was born in Keelung, Taiwan in 1992. He graduated from Taipei Municipal Jianguo High school in 2010. In 2014, he graduated with an overall class rank number 3 out of 150 students from National Taiwan University in Taipei, Taiwan with a Bachelor of Science degree in Mechanical Engineering.

ACKNOWLEDGEMENT

I would like to thank my family for their incessant and full support. I would also like to thank my committee members for their time, guidance, and mentorship. Lastly, I would like to thank all members in Hernandez Lab for their help and advice. A two year journey at Cornell cannot be so memorable and invaluable without all you.

TABLE OF CONTENTS

Chapter 1. Stress Analysis of the Bacteria Submitted to Extrusion Loading

1.1 Introduction

1.1.1 Bacterial Anatomy

All living organisms can be broadly categorized into either prokaryotic or eukaryotic cells. Animals, plants, and fungi belong to eukaryotes. Bacteria, on the other hand, are prokaryotes. Prokaryotes are fundamentally different from eukaryotes in that they lack membrane bound organelles. The most obvious example is that prokaryotes lack nucleus. Bacteria exist in unicellular form, although being unicellular is not an attribute in distinguishing between prokaryotes and eukaryotes. Yeast, for instance, is a single-celled organism but belongs to eukaryotes.

The cell wall is the major stress-bearing component in bacteria [1]. The primary function of the cell wall is to maintain cell shape and structurally support bacteria. The cell wall is made of peptidoglycan, which is composed of polysaccharide chains cross-linked by peptide chains. The peptidoglycan is mesh-like and does not limit the passage of small molecules.

The cytoplasm is enclosed by the cell membrane. The cytoplasm is composed of water and is the solvent for bacterial components responsible for metabolism, growth, and replication of genetic materials in the cells. In addition, enzymes, wastes, nutrients, ions, gases, and other

molecules are distributed in the cytoplasm. The most easily observable structure inside the cytoplasm is the nucleoid, which is a compact region of bacterial genomic materials.

The cell membrane encloses the cytoplasm, and is sandwiched between the cytoplasm and the cell wall. The central role for the cell membrane is to regulate transport of molecules into and out of the cell. The bacterial cell membrane is a lipid bilayer consisting of phospholipids. The amphipathic nature of phospholipids, with hydrophilic tails and hydrophobic heads, enables self-assembly. The lipid constituents in the cell membrane make it automatically permeable to gases and small lipophilic molecules. Additionally, many proteins in the cell membrane are involved in the active transport to control the flows of molecules across the cell membrane.

The most common mechanical loads experienced by bacteria in their natural environment is osmotic pressure. Osmotic pressure arises due to the ionic concentration (osmolarity) difference between the cytoplasm and surrounding media. Normally, bacteria possess positive osmolarity in that the cytoplasm has greater ionic concentration than environment. With the presence of the semipermeable cell membrane that is less a barrier to water than to ions, the concentration gradient of water drives the water molecules from media to the bacterial cytoplasm, expanding the membrane. Osmotic pressure is defined as the pressure sufficient to prevent the influx of water to cells [2]. In bacteria, as water diffuses into the cytoplasm, the cell membrane can expand only to a degree that it is firmly in contact with the surrounding cell wall. Additional

water influx results in mechanical stress buildup in the cell wall. The pressure applied on the cell wall due to osmolarity difference is referred to as the turgor pressure.

One of the difficulties for survival of bacteria is the constantly changing osmolarity in natural environment. Mechanosensitive (MS) ion channels on the cell membrane are believed to be crucial for bacteria to survive in a wide range of external osmolarities. MS ion channels prevent cells from bursting in hypotonic solution (lower osmolarity in the solution than in the cytoplasm) by sensing the mechanical tensile stress on the cell membrane and allowing transmission of water [3].

Cytoskeletal elements are major components of mechanotransduction in eukaryotic cells Bacteria do not have cytoskeletal elements but instead have cytoskeletal homologues. The cytoskeleton homologues are filamentous proteins attached to the cell membrane. MreB, FtsZ, and CreS are the most studied cytoskeletal-like filaments. MreB has been shown to contribute to the whole cell stiffness. Depolymerization of MreB in *Escherichia coli* resulted in 30% reductions in their flexural rigidity in mechanical bending tests [4]. MreB molecules also guide peptidoglycan syntheses and insertions and help maintain the rod shape of *E. coli*. *E. coli* depleted with MreB grew into spherical morphology [5]. FtsZ is an important element in cell division. FtsZ molecules localize at mid cell to form a division ring, which then is postulated to exert a contraction force that pinches the cell into two halves [6]. The molecule CreS is required for the

crescent shape in *Caulobacter crescentus*. CreS exerts compressive force on the sidewall of the bacteria, resulting in gradients in cell lengthening that lead to a curved shape [7].

Bacteria are broadly classified as Gram positive or Gram negative by the degree to which the bacteria retain crystal violet dye in Gram stain test. One structural difference between the two groups is that Gram negative bacteria have a thinner peptidoglycan layer than Gram positive bacteria. Next, Gram negative bacteria contain a second cell membrane outside the cell wall. The outer membrane features lipopolysaccharides. Lipopolysaccharides are anchored to the outer membrane and project into the surroundings. Additionally, the outer membrane contains the transport channels called porins that make it more permeable than the inner membrane. The space between the inner and the outer membrane is known as the periplasm or the periplasmic space.

1.1.2 Mechanical Characterization of *Escherichia coli*

Escherichia coli are rod-shaped Gram negative bacteria. In mechanical models, *E. coli* have been modelled as thin-walled pressure vessels. In our analyses we assume a simplified rod-like geometry including a cylinder with two hemispherical end caps. Turgor pressure is present in bacteria that inflates the cell wall and produces tensile mechanical stress in the cell envelope. As a pressure vessel it is appropriate to use the thin walled assumption as the radius of *E. coli* is two orders of magnitude larger than the cell envelope thickness.

The cell envelope of *E. coli* is an elastic anisotropic material. *E. coli* have been shown to behave elastically when subjected to transient forces [8, 9]. In addition, the cell envelope Young's modulus in the circumferential direction is two times higher than that in the longitudinal direction [10, 11]. Young's modulus has been reported in a range from 2 to 220 MPa (Table 1.1), but the Poisson's ratio is yet to be measured.

Table 1.1 Reported cell envelope Young's moduli of *Escherichia coli*. Some measurements using atomic force microscopy indentation do not specify the direction of obtained Young's modulus.

Young's Modulus (MPa)		**Method**	**Reference**
Longitudinal	Circumferential		
23.0	49.0	Atomic Force Microscopy Indentation	Deng *et al.* [10]
25.0	45.0		Yao *et al.* [11]
12.8			Abu-Lail *et al.* [12]
3.0			Cerf *et al.* [13]
0.4			Chen *et al.* [14]
221.4			Eaton *et al.* [15]
2.6			Perry *et al.* [16]
34.8	–	Optical Trapping	Wang *et al.* [4]
31.8	–	Fluidic Bending	Amir *et al.* [9]
28.0	–		Auer *et al.* [17]
21.7	–		Caspi [18]
50.0 – 150.0	–	Agarose Gel Encapsulation	Tuson *et al.* [19]
30.0	–	Analytical Solution	Boulbitch *et al.* [20]
6.1 – 17.5	62.5 – 66.3	Computational Solution	Gumbart *et al.* [21]

1.1.3 Extrusion Loading and Bacteria

The current work involves mechanical characterization of stresses and strains induced using an experimental technique known as "extrusion loading [22]." Extrusion loading involves flowing bacteria in liquid media into tapered constrictions. The bacteria trapped in the constrictions experienced a difference in fluidic pressure from upstream to downstream. Meanwhile the sidewalls of the bacteria were subjected to frictional force and normal force related to contact with the walls of the tapered channels (Figure 1.1A).

Extrusion loading is implemented using a microfluidic device that consists of a network of bypass channels in parallel with tapered channels (referred to as 'traps') (Figure 1.1B). A syringe pump is used to inject media into the device through the inlet channel. A pressure sensor is placed at the inlet of the bypass channel to record the applied pressure. As bacteria in media are flowed into the device, they either flow through the bypass channels or enter a trap. The cross-section of traps at the entrance is larger (1.4 μm x 1.4 μm) than the average width of *Escherichia coli* or *Bacillus subtilis* (~1 μm). At the exit of traps, the cross-section is smaller (0.25 μm x 1.2 μm) than the bacteria. We denote the entrance side of traps as upstream and the exit side as downstream. The device was made from fused silica as glass which is considerably stiffer than bacteria and has optical clarity for imaging the cells inside the device (Figure 1.1B, inset).

We determined the local hydrostatic pressures at the two ends of each trapped bacteria using hydraulic circuit calculations [22]. The channels in the device were represented by hydraulic resistors. The hydraulic resistance is defined as the pressure drop across a channel divided by the flow rate within it. The resistance of a channel with rectangular cross-section, R_h was determined from the Hagen-Poiseuille law as [23]:

$$R_h = \frac{\delta P}{Q} = \frac{12\eta l}{h^3 w} \tag{1.1}$$

, where δP is the pressure drop, Q is the flow rate, η is the viscosity of the media, l is the length, h is the height, and w is the width of the channel. Analogous to electrical circuits, we can calculate the total hydraulic resistance of resistors in series or in parallel. The pressure at the upstream end, P_u and the pressure at the downstream end, P_d of a trapped cell are thus obtained after using the hydraulic circuit calculations. The pressure difference applied on a trapped cell is $\Delta P = P_u - P_d$. The average pressure experienced by a trapped cell is $P_{ave} = (P_u + P_d)/2$. Each functional device contains sets of traps along a bypass channel to achieve a range of pressure difference (Figure 1.1B).

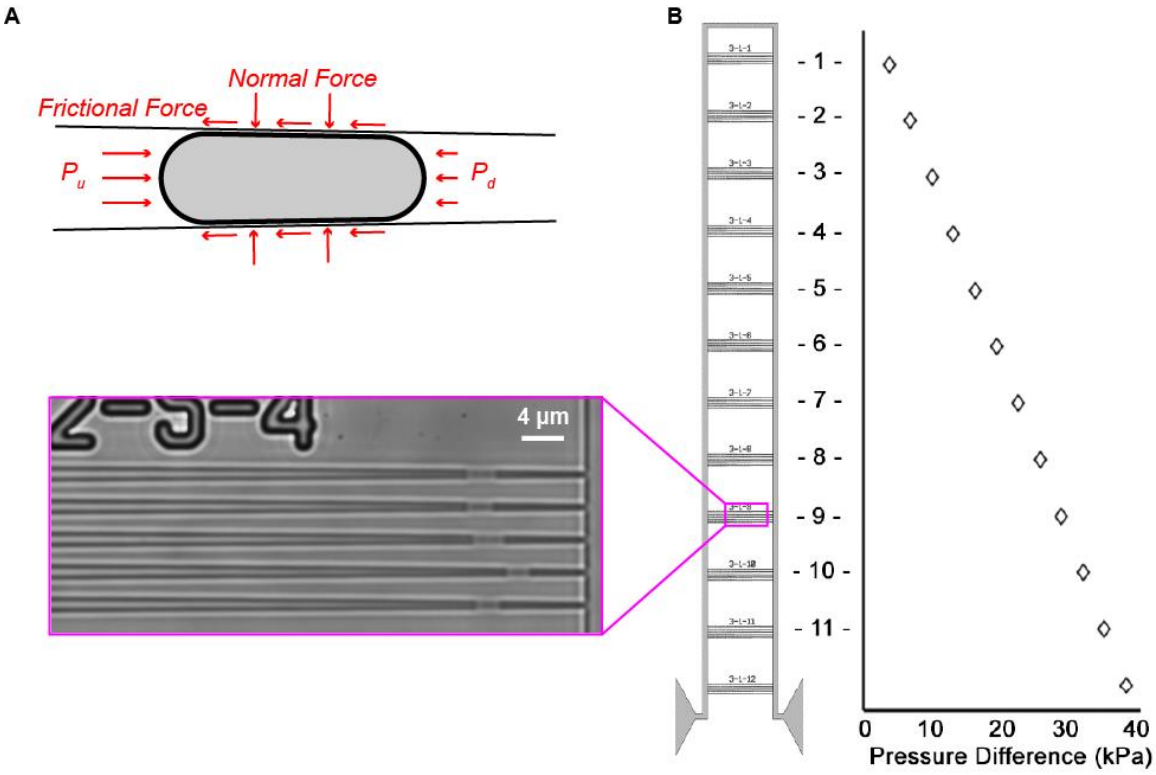

Figure 1.1 Extrusion loading and the microfluidic device. (A) External loads applied on a trapped cell under extrusion loading. (B) Sets of taper channels along a bypass channel and their corresponding pressure difference (copyright courtesy of M.F. Roberts). (Inset) A microscopy image of the trapped bacteria in taper channels.

1.1.4 Research Question

Our research goal is to analyze the stress and strain states on the cell envelope under extrusion loading as a means of understanding the effects of mechanical stress and strain on the CusCBA efflux system (M.F. Melanie & L.A. Genova (2018), Paper submitted for publication). CusCBA is a tripartite Cu^+ and Ag^+ efflux complex in Gram negative bacteria that traverses across the thickness of the cell envelope. CusC is located on the outer membrane, CusB is located in the periplasm, and the CusA is located on the inner membrane. When the three assemble together, CusCBA extrudes Cu^+ and Ag^+ in the cell. It has been shown that CusCBA complex

exists in a dynamic equilibrium between the assembled state and the disassembled state [24]. Recently we have found that the disassembly rate of CusCBA in *E. coli* increased as extrusion loading applied on the bacteria increased. This suggested that the bacterial efflux was affected by mechanical loading. We therefore developed mechanical models to characterize the stress and strain states of the bacteria submitted to extrusion loading.

1.2 Analytical Model

The analytical model in this section was created and described in detail and provides information on the stress and strain states in a bacterium submitted to extrusion loading. The experiments relevant to the derivations of the analytical model is introduced below.

1.2.1 Stepwise Increases in Extrusion Loading Experiments

E. coli suspended in liquid media were submitted to extrusion loading (see section 1.1.3) with an initial P_{ave} of 46 kPa (ΔP range: 15–49 kPa). Images of the bacteria were collected using bright field microscopy (0.108 μm per pixel). The applied fluid pressure was increased and a new bright field image of the same bacteria was collected (Figure 1.2A). The process was repeated resulting in an image of each cell at three different magnitudes ΔP. Stepwise loading occurred over a short timeframe (~19 min) at room temperature, so that changes in cell length were not influenced by growth processes. Increases in applied ΔP resulted in movement of the bacteria further into the tapered channels leading to a reduction in cell width (Figure 1.2B). Additionally,

cell length increased (Figure 1.2C). These observations show that increased magnitude of extrusion loading results in reductions in tensile hoop strains, increases in tensile strain in the longitudinal direction and a net reduction in cell volume (Figure 1.2D).

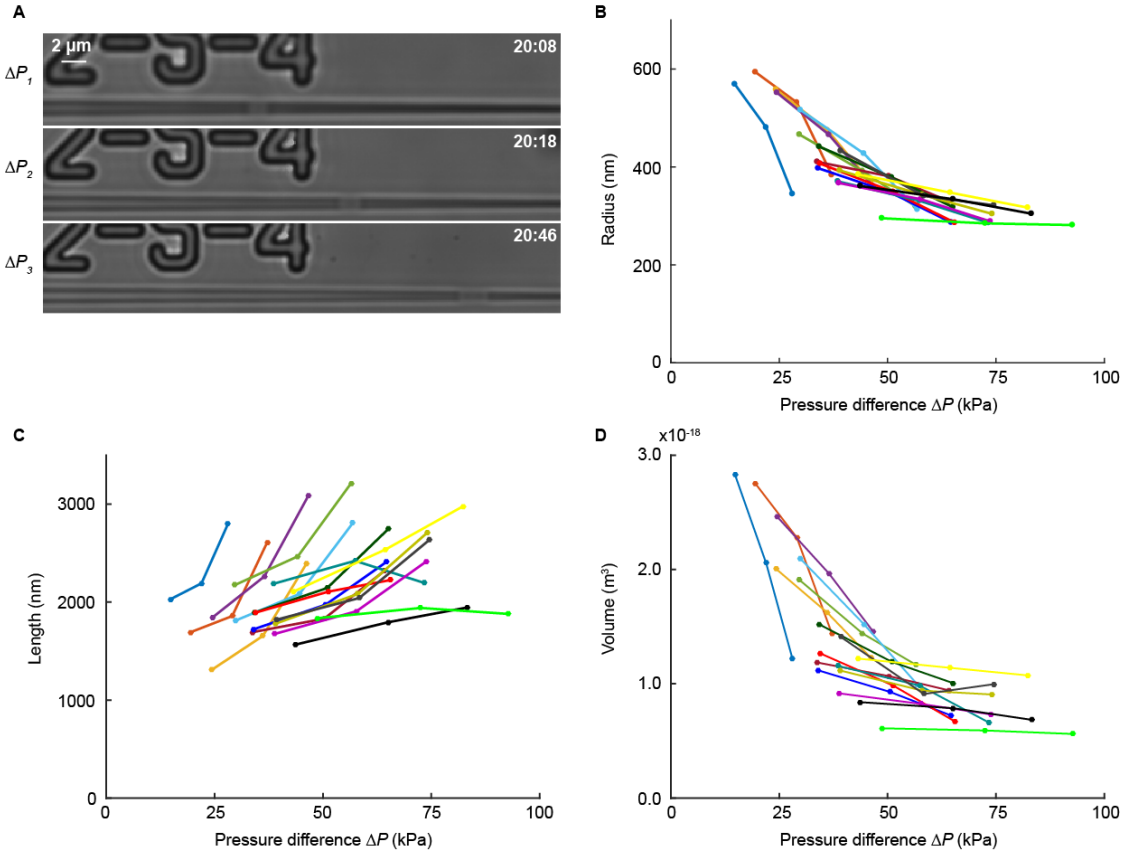

Figure 1.2 Changes in cell dimensions in *E. coli* submitted to stepwise increases in extrusion loading. (A) Bright field images of the same bacteria submitted to three different magnitudes of extrusion loading. (B) The mid cell radius of bacteria at each of the stepwise increases in pressure are shown (n = 17, lines connect measures of the same cell). (C) The length of bacteria at each of the stepwise increases in pressure are shown. (D) The volumes of bacteria submitted to stepwise increases in ΔP. Volume is calculated assuming a cylindrical shape of each bacteria.

1.2.2 Methods

An analytical model based on force balance and transversely isotropic constitutive laws is derived by Srivastava [25] and elaborated here. The analytical model assumes an axisymmetric

cell geometry. The cell contains a turgor pressure, P_t associated with osmolarity and is submitted to an upstream fluidic pressure, P_u and a downstream fluidic pressure, P_d. The difference between upstream and downstream pressure ($P_u - P_d$) is the pressure difference ΔP. A normal pressure, P_{wall} resists the internal cell pressure at the channel wall and a frictional pressure, τ associated with contact to the cell envelope is also present (Figure 1.3A).

The stress and strain, and the change in turgor pressure of a bacterium at two loading configurations (ΔP_1 and ΔP_2) are considered (Figure 1.3A). The cylindrical portion of the bacterium (AA' to BB' in Figure 1.3A) is referred to as 'trunk' and the ends as 'caps'. The cell envelope thickness is denoted by t. As the taper angle α in the microfluidic channel is very small (~0.5°), we assume uniform radius for the trunk.

We denote the displacement of the point X in the cell envelope as it moves from configuration 1 to configuration 2 as u, such that $x = X + u$. As the cell moves from configuration 1 to configuration 2, the axial strain ε_a and the hoop strain ε_h in the cell envelope are given by:

$$\varepsilon_a = du(X)/dX = u'(X) \tag{1.2}$$

$$\varepsilon_h = (r_2 - r_1)/r_1 \tag{1.3}$$

We assume small strains and thus bending in the cell envelope is neglected [26]. The incremental tensile axial stress $\delta\sigma_a$ and the incremental tensile hoop stress $\delta\sigma_h$ between two configurations are given as:

$$\sigma_{a2} = \sigma_{a1} + \delta\sigma_a \tag{1.4}$$

$$\sigma_{h2} = \sigma_{h1} + \delta\sigma_h \tag{1.5}$$

The cell envelope is modeled as a linear elastic transversely isotropic material [10, 11] with hoop Young's modulus, E_h on the isotropic plane, and the axial Young's modulus, E_a. The anisotropic coefficient $\gamma = E_h/E_a$ describes the relationship between the two. υ_{ha} is the Poisson's ratio in the axial direction. The relationship between incremental stresses, $\delta\sigma_a$ and $\delta\sigma_h$ and strains, ε_a and ε_h is given by the constitutive laws as:

$$\delta\sigma_a = \frac{E_h}{\gamma - {\upsilon_{ha}}^2}(\varepsilon_a + \upsilon_{ha}\varepsilon_h) = \frac{E_h}{\gamma - {\upsilon_{ha}}^2}\left[u'(X) + \upsilon_{ha}\frac{r_2 - r_1}{r_1}\right] \tag{1.6}$$

$$\delta\sigma_h = \frac{E_h}{\gamma - {\upsilon_{ha}}^2}(\upsilon_{ha}\varepsilon_a + \gamma\varepsilon_h) = \frac{E_h}{\gamma - {\upsilon_{ha}}^2}\left[\upsilon_{ha}u'(X) + \gamma\frac{r_2 - r_1}{r_1}\right] \tag{1.7}$$

The local force balance in the hoop direction (Figure 1.3B) in the two configurations is:

$$\sigma_{h1}(X) = \frac{r_1}{t}[P_{t1} - P_{wall1}(X)] \tag{1.8}$$

$$\sigma_{h2}(X) = \frac{r_2}{t}[P_{t2} - P_{wall2}(X)] \tag{1.9}$$

The balance of longitudinal forces at a point X on the cell (Figure 1.3C) is obtained from a force balance, assuming a constant Coulomb friction coefficient f between the cell and the channel walls and characterizing $\tau = fP_{wall}(X)$ for both configurations as follows:

$$\frac{d\sigma_{a1}(X)}{dX} = \frac{f}{t}P_{wall1}(X) + \frac{\alpha}{r_1}[\sigma_{a1}(X) - \sigma_{h1}(X)] \tag{1.10}$$

$$\frac{d\sigma_{a2}(X)}{dX} = \left\{\frac{f}{t}P_{wall2}(X) + \frac{\alpha}{r_2}[\sigma_{a2}(X) - \sigma_{h2}(X)]\right\}(1 + u') \tag{1.11}$$

, where we have removed higher order, incremental terms.

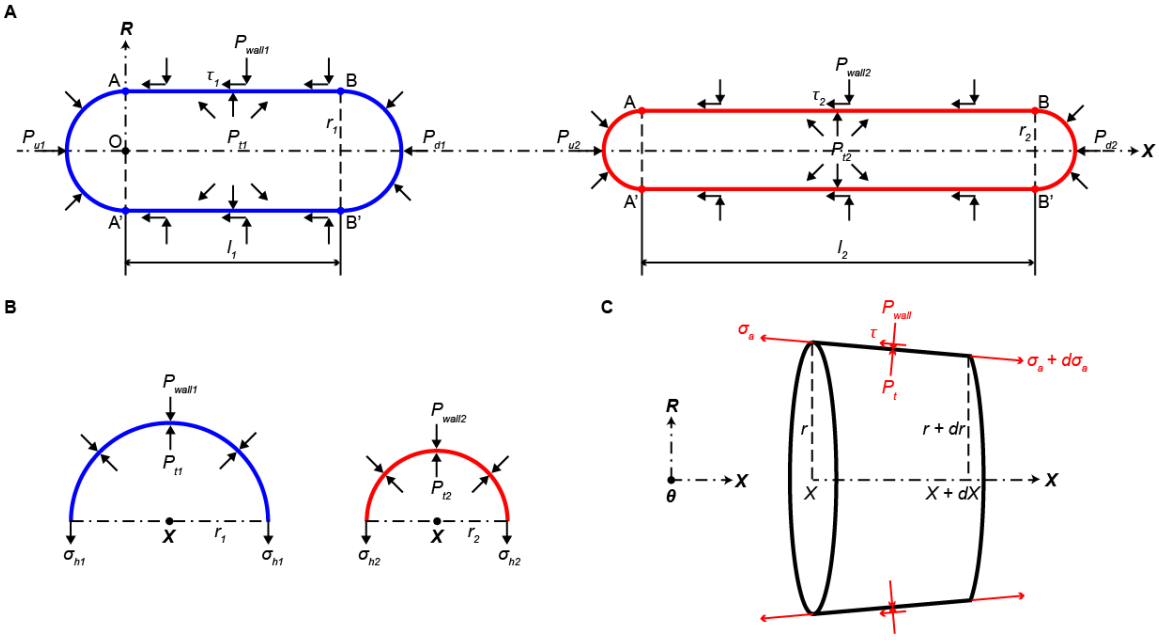

Figure 1.3 Free body diagrams of a bacterium under extrusion loading. (A) Schematic of a bacterium trapped inside a channel at two applied pressures. The blue (left) bacterium is at lower applied pressure, and the red (right) one is at higher applied pressure. (B) The local force balance in the hoop direction. The black dots denote the axial axis. (C) The local force balance of a segment of a trapped bacterium in the longitudinal direction.

Considering the cell as a single body, the longitudinal forces from the pressure difference must be balanced by wall pressure and friction resulting in the following equations:

$$\hat{P}_{wall1} = \frac{1}{l_1}\int_0^{l_1} P_{wall1}(X)dX = \frac{r_1 \Delta P_1}{2l_1(f+\alpha)} \tag{1.12}$$

$$\hat{P}_{wall2} = \frac{1}{l_2}\int_0^{l_1} P_{wall2}(X)(1+u')dX = \frac{r_2 \Delta P_2}{2l_2(f+\alpha)} \tag{1.13}$$

The change in turgor pressure between two configurations can be assessed from the force balance in the hoop direction. By subtracting Equation (1.8) from Equation (1.9), integrating both sides of the equation across the length of the cell, and substituting Equation (1.7), (1.12), and (1.13) we achieve:

$$P_{t2} - P_{t1} = \frac{r_1(\Delta P_2 - \Delta P_1)}{2l_1(f+\alpha)} + \frac{tE_h}{r_1(\gamma - {\upsilon_{ha}}^2)}\left(\upsilon_{ha}\frac{l_2 - l_1}{l_1} + \gamma\frac{r_2 - r_1}{r_1}\right) \tag{1.14}$$

The axial strain and incremental axial stress distributions can now be readily calculated. Differentiating Equation (1.4) and replacing the resulting terms with Equation (1.6), (1.8 – 1.11), and (1.14) give us:

$$u'' + Qu' = M \tag{1.15}$$

, where $M \triangleq \frac{(\gamma - {\upsilon_{ha}}^2)f}{tE_h}\left[\frac{r_1(\Delta P_2 - \Delta P_1)}{2l_1(f+\alpha)} + \frac{tE_h \upsilon_{ha}\frac{l_2 - l_1}{l_1}}{r_1(\gamma - {\upsilon_{ha}}^2)}\right] + \frac{\alpha(\upsilon_{ha} - \gamma)\varepsilon_h}{r_1}$ and $Q \triangleq \frac{(f+\alpha)\upsilon_{ha} - \alpha}{r_1}$.

Recognizing from cell geometry that, $r_2 - r_1 = -u(0)\cdot\alpha$ and $u(l_1) - u(0) = l_2 - l_1$, the distribution of axial strain is expressed as:

$$\varepsilon_X = u'(X) = \frac{M}{Q} - \frac{Ml_1 - Q(l_2 - l_1)}{1 - e^{-Ql_1}}e^{-QX} \tag{1.16}$$

The incremental axial stress is then obtained from Equation (1.6) and (1.16)

1.2.3 Results

An expression for the change in turgor pressure between two configurations is obtained in Equation (1.14). Substituting values for pressure, radius and Young's moduli within the experimental range, the right hand side of Equation (1.14) is always positive, i.e. increases in pressure difference result in increases in internal pressure. The increase in turgor pressure is consistent with observed reductions in cell volume during stepwise extrusion loading (Figure 1.2D) in that volume loss is most likely predominately water (the cell remains viable after loading). A reduction in water content would be expected to increase osmolarity and thereby increase turgor pressure.

The axial strain (Equation 1.16) can be shown to increase monotonically from the upstream end ($X = 0$) to the downstream end ($X = l_1$) of the trunk if we solve the longitudinal force balance at two end caps and use the results from it. As a function of the axial strain, the incremental axial stress likewise exhibits a monotonically increasing pattern along the length of the trunk.

We conclude from this analytical analysis that during extrusion loading the axial strain and stress are distributed in an increasing pattern from the upstream end to the downstream end and that extrusion loading results in increased turgor pressure.

1.3 Finite Element Model

The analytical model above, while providing insight into the stresses and strains generated by extrusion loading, has limited utility for quantitative analysis as many of the variables have not been well defined experimentally. Here we generate finite element models to assess the complete state of stress in a cell envelope under extrusion loading. The experiments used for the derivations of the finite element model are explained below.

1.3.1 Relationship between Cell Morphology and Applied Extrusion Loading

A total of 1366 *E. coli* BW25113 bacteria were submitted to extrusion loading and a single image of each cell was obtained as part of another experiment. The applied pressure differences (ΔP range: 1–49 kPa) were achieved at using multiple days of experiments using two different average pressures (P_{ave}: 12.5 and 30.0 kPa). The cell length and mid cell width of each trapped cell were measured (Figure 1.4).

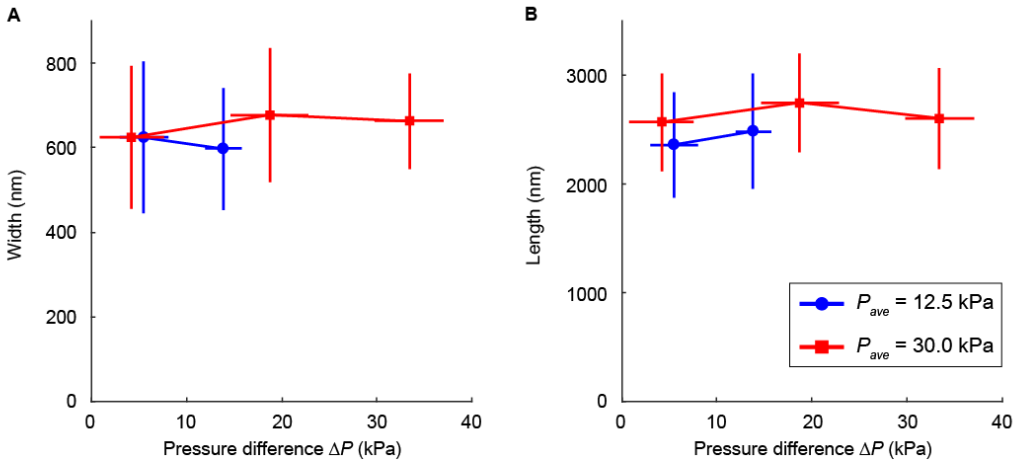

Figure 1.4 Cell dimensions in experiments. Cell length and width are binned according to its pressure difference (ΔP: 0−10, 10−25, 25+ kPa) and average pressure (P_{ave}: 12.5, 30.0 kPa). The x- and y-error bars are s.d.

1.3.2 Methods

Characterization of the stress and strain state in the cell envelope during extrusion loading was performed using a nonlinear finite element analysis. A finite element model of a bacterium submitted to extrusion loading was developed using Abaqus (CAE 6.9-EF2, Dassault Systems, Providence, RI). An axisymmetric model of the cell envelope using solid elements was generated. The use of solid elements constrains the model to considering situations with a positive turgor pressure (a reasonable assumption given the increases in internal pressure during extrusion loading, see above). The trunk of the cell envelope was modeled using transverse isotropy (see section 1.2.2). The Poisson's ratios on the isotropic plane was 0.3, and the Poisson's ratio in the hoop-axial direction was 0.34 [21]. The end caps were assigned isotropy, with the Young's modulus as the average of the Young's moduli in the hoop and longitudinal direction in the trunk and the Poisson' ratio as 0.3. Channel walls were represented by rigid surfaces with dimensions determined from the microfluidic device. Contact between the cell envelope and the channel walls was simulated using a surface-to-surface contact. Coulomb friction was applied between the cell envelope and channel walls, with friction coefficients estimated from global force balance in the longitudinal direction of a trapped cell envelope. Each finite element model consisted of 103,680 four-node bilinear quadrilateral elements (16 elements across the cell

thickness, CAX4 elements with geometric nonlinearities included). The thickness of the cell envelope, t was 4 nm [10, 11].

Extrusion loading was simulated in two steps (Figure 1.5A). In the initial step the cell envelope was inflated with a turgor pressure characteristic of the free-floating state, $P_{t,0}$. Although reports of turgor pressure and cell envelope Young's moduli vary dramatically in the literature, cell width is highly conserved [27] and has small variability in the strain of *E. coli* used in this experiment (1.13 ± 0.14 μm) [28]. The unstressed width, turgor pressure and the cell envelope Young's modulus were varied iteratively and the combinations of these three parameters that achieved a final width similar to that of free-floating *E. coli* (known) were determined.

In the second step of the simulation, upstream and downstream pressure was applied and the internal pressure was increased to $P_{t,load}$. Stabilization control was used in Abaqus to allow for small rigid body motion of the cell envelope within the channels.

Table 1.2 Ranges of tested parameters for the cell envelope in the finite element model.

Parameter	Definition	Parameter Range	Reported Range
E_a	Axial Young's Modulus	20 – 60 MPa	20 – 150 MPa [4, 9-11, 17-19]
$P_{t,0}$	Turgor Pressure Prior to Extrusion Loading	100, 150, 200 kPa	30 – 300 kPa [10, 29, 30]
$P_{t,load}$	Turgor Pressure during Extrusion Loading	$P_{t,0}$ – 500 kPa	–
l_0	Unstressed Cell Length	1000 – 2400 nm	–

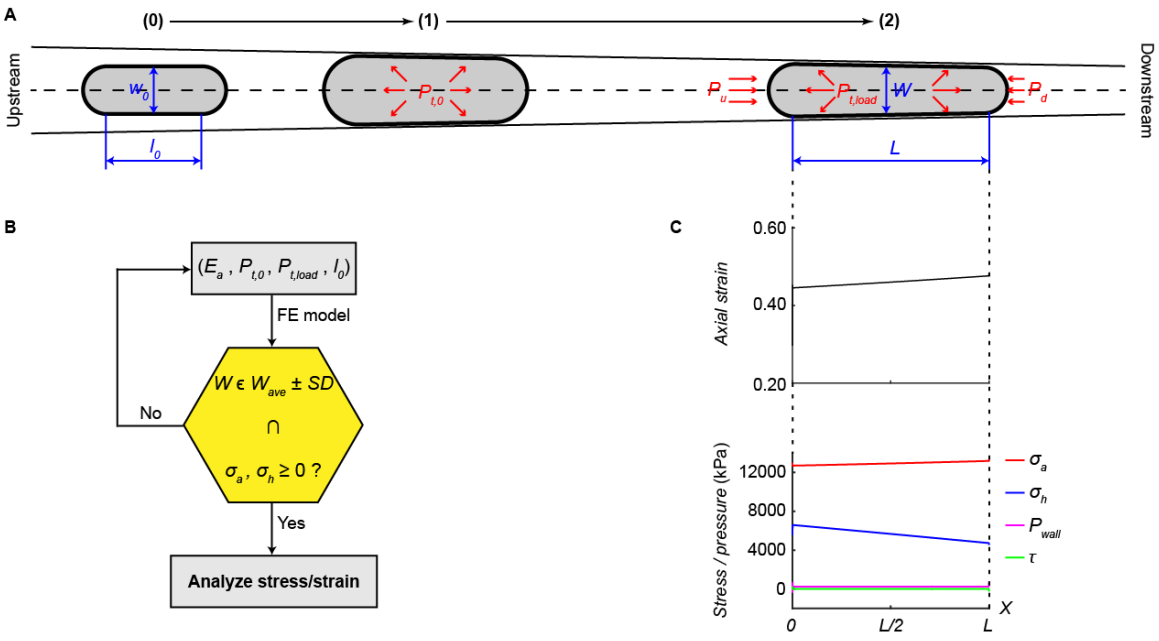

Figure 1.5 Parametric finite element models. (A) Schematic of the finite element model. Numbers mark the steps in a simulation. (B) Flowchart of the parametric analysis. Finite element model outputs cell width *W*, which is compared to the experimental width (Table 1.3). Axial and hoop stresses must be tensile. Simulations consistent with these two criteria are considered consistent with experimental findings. (C) An example of the simulation stress and strain distributions that match experimental findings in which E_a = 25 MPa, $P_{t,0}$ = 150 kPa, $P_{t,load}$ = 270 kPa, l_0 = 1200 nm, and the applied pressure is ΔP = 20 – 30 kPa, P_{ave} = 30.0 kPa.

As many of the parameters used in the finite element model have not yet been well defined experimentally (Table 1.2), we performed a parametric analysis to identify the combination of values that result in deformations similar to what are seen experimentally (Figure 1.5B). Key input parameters for the model include Young's moduli, initial turgor pressure, and turgor pressure after deformation. Finite element model results were compared to cell width and length obtained in experimental studies at known pressure differences ΔP (data from Table 1.3). Cell width is not highly variable in this strain of *E. coli* but cell length varies considerably

depending on the state of the cell cycle. For this reason, final deformed cell width was used as the primary indicator that a simulation was consistent with experimental findings. In the parametric analysis, Young's modulus in the hoop direction, E_h is two times greater than that in the axial direction, E_a [10, 11]. The turgor pressure within a cell during extrusion loading, $P_{t,load}$ is equal or greater than that prior to extrusion loading, $P_{t,0}$ (see section 1.2.3). The unstressed cell length, l_0 can also affect how far a cell traveled downstream and thus the final cell width, and was included as a free variable. Although the amount of initial contact between the cell envelope and the channel walls following the first step of the simulation can vary based on the initial position of the cell within the tapered channel, variation in the starting position had little effect on final cell width (additional 6 simulations indicated no difference in final cell width when initial cell position varied by more than ± 30%).

Table 1.3 Applied pressure differences and cell dimensions from Figure 1.4 are shown. The parametric analysis identifies sets of unknown parameters (turgor pressure, Young's modulus, and unstressed cell length) that result in cell width similar to that seen experimentally. *W* is expressed at mid cell and *L* is the length of the cell trunk (not including caps).

P_{ave} (kPa)	ΔP (kPa)	*n*	$P_{u,ave}$ (kPa)	$P_{d,ave}$ (kPa)	$W_{ave} \pm SD$ (nm)	$L_{ave} \pm SD$ (nm)
12.5	6 – 10	111	16.46	8.53	572 ± 155	2306 ± 470
	10 – 20	381	19.44	5.55	598 ± 145	2486 ± 528
30.0	10 – 20	95	37.73	22.25	684 ± 165	2762 ± 438
	20 – 30	146	42.16	17.82	697 ± 134	2617 ± 467
	30+	296	47.28	12.70	645 ± 104	2596 ± 457

1.3.3 Results

The stress and strain states from the finite element simulations (Figure 1.5C) were consistent with the analytical results (see section 1.2.3). The axial stress increases monotonically from the upstream end to the downstream end along the cell length. The hoop stress is less tensile at the downstream end. The normal pressure exerted by channel walls is increased at the downstream end. The shear stress is relatively constant and is more than three orders of magnitude smaller than the normal stresses. The axial strain is increased at the downstream end.

Additionally, the turgor pressure, $P_{t,load}$ in deformed cells was correlated with ΔP in simulations that matched experimental results (Table 1.4), which is in agreement with the conclusion from the analytical model (see section 1.2.3).

Table 1.4 An example of ranges of parameters under the same cell wall Young's modulus and initial turgor pressure that match experimental findings (i.e. achieve final cell width within 1 SD of the measured values).

P_{ave} (kPa)	ΔP (kPa)	E_a (MPa)	$P_{t,0}$ (kPa)	$P_{t,load}$ (kPa)	l_0 (nm)
30.0	10 − 20	25	150	150 − 230	1400 − 2400
	20 – 30	25	150	190 − 280	1200 − 2000
	30+	25	150	260 − 300	1200 – 1600

In simulations that matched experimental results (Table 1.4), extrusion loading causes increased axial stresses, increased shear stresses, reduced hoop stresses, and more compressive radial stresses (Figure 1.6).

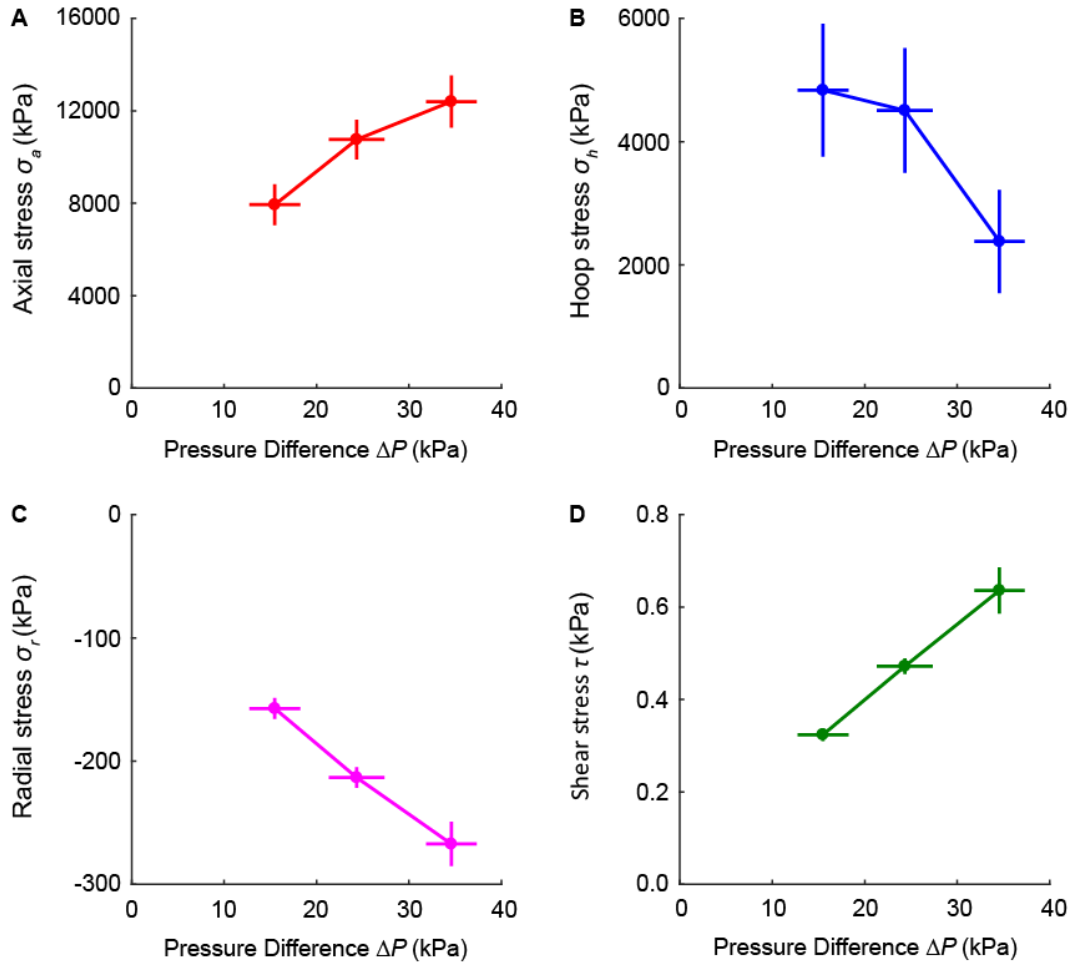

Figure 1.6 Stress state of the bacteria submitted to extrusion loading. The change in stresses in a cell envelope following an increase in magnitude of extrusion loading. The simulation stresses are obtained at mid cell and at the mid layer of a cell envelope. Shown here are the results for simulations with E_a = 25 MPa, $P_{t,0}$ = 150 kPa (Table 1.4). X-error bars are s.d.; y-error bars are 95% confidence interval.

Experimental results indicated similar responses of *E. coli* to both extrusion loading and loading through gel encapsulation. The stress state of bacteria under extrusion loading was then compared to that of bacteria under agarose gel encapsulation (Table 1.5). During elongation of a single cell, cell envelope material is added thereby increasing cell length. When encapsulated in a stiff gel, the longitudinal extension of the cell during growth is constrained. The cell envelope is

normally under tension due to turgor and the presence of the gel results in a reduction in longitudinal tensile stress in the bacterial cell envelope [19]. As there is typically no expansion of *E. coli* in the hoop direction, hoop stress remains identical to that present in a free-floating cell. We modeled the bacteria using a transversely isotropic linear elastic constitutive model (see section 1.3.2) with applied turgor pressure, $P_{t,0}$ and longitudinal compressive pressures, P_{gel} yielded from the growth constraints (Figure 1.7C, inset).

Table 1.5 The responses of stress to increases in external loading of the two loading modes. "–" denotes no change.

Loading Mode	σ_a	σ_h	σ_r	τ	σ_{hyd}	τ_{oct}
Extrusion Loading	↑	↓	↓	↑	–	↑
Agarose Gel Encapsulation	↓	–	–	–	↓	↑

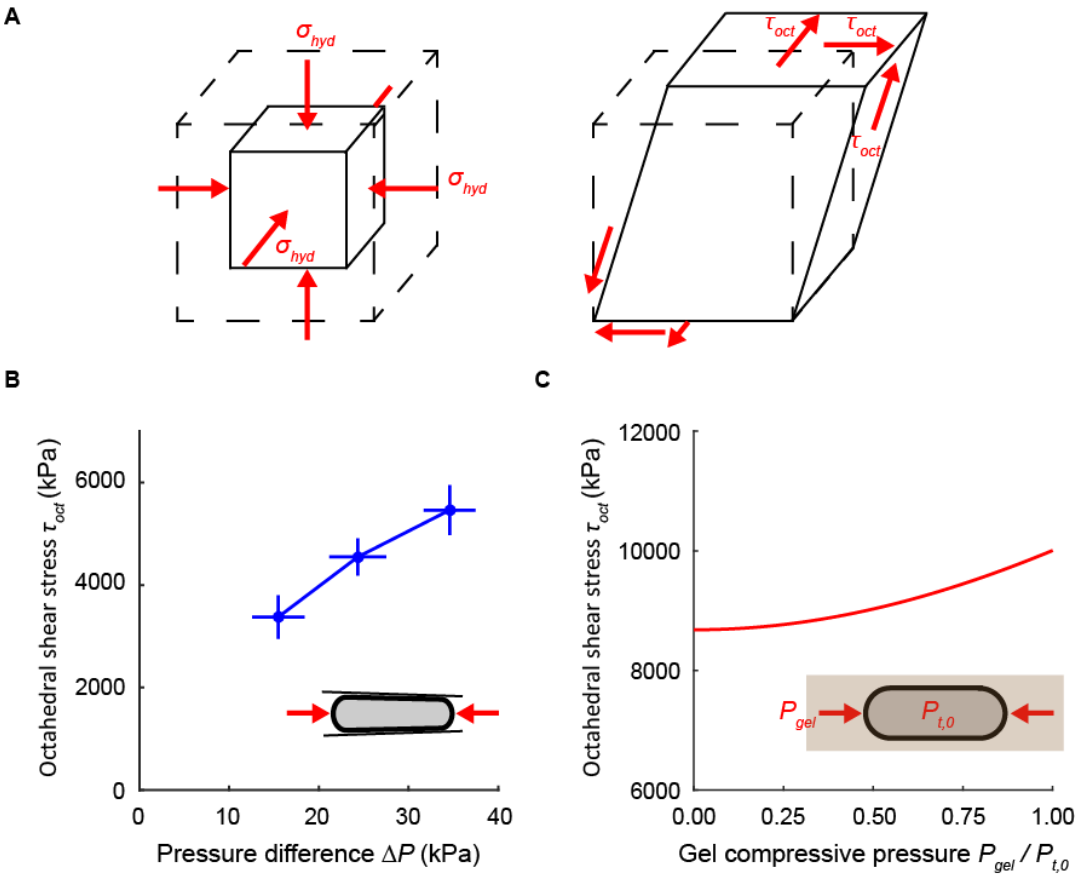

Figure 1.7 Octahedral shear stress in bacteria under extrusion loading and agarose gel encapsulation. (A) The effects of the normal (hydrostatic stress, left) and shear (octahedral shear stress, right) stress on an infinitesimal element located on the octahedral plane. (B) The change in the octahedral shear stress in a cell envelope following an increase in magnitude of extrusion loading. Shown here are the results for simulations with E_a = 25 MPa, $P_{t,0}$ = 150 kPa (Table 1.4). X-error bars are s.d.; y-error bars are 95% confidence interval. (C) The analytical solution of the octahedral shear stress in a cell envelope following an increase in magnitude of compressive pressure from the surrounding gel. The parameters used are E_a = 25 MPa, $P_{t,0}$ = 150 kPa.

Although the normal stresses in the two loading modes are very different, decomposing the three dimensional stress state into hydrostatic and octahedral shear components shows that both loading modes result in increases in octahedral shear stress (Figure 1.7B and C). The hydrostatic stress is related to volume change of an infinitesimal element in a material; the

octahedral shear stress is related to shape change under constant volume of an infinitesimal element oriented in the principal coordinate system of a material (Figure 1.7A).

1.4 Conclusions

The mechanical models suggested that bacteria submitted to extrusion loading experienced increases in tensile axial stress and shear stress and decreases in tensile hoop stress. Additionally, extrusion loading caused increases in compressive radial stress (associated with increased internal pressure). Within the cell envelope, axial stress was more tensile at the downstream end of the trunk, but hoop stress was less tensile at the downstream end. Shear stress was uniformly distributed in the trunk and had a magnitude that is negligible compared to the normal stresses. Extrusion loading led to increases in turgor pressure.

The octahedral shear stress in bacteria under extrusion loading and agarose gel encapsulation both increased but other normal stresses did not respond similarly in the two loading modes, indicating that the octahedral shear stress is responsible for the observed disassembly rate change of CusCBA in *E. coli*.

1.5 Reference

[1] D.M. Morris, G.J. Jensen, Annu Rev Biochem, 77 (2008) 583-613.
[2] L.N. Csonka, Microbiol Rev, 53 (1989) 121-147.
[3] B. Martinac, J Cell Sci, 117 (2004) 2449-2460.
[4] S.Y. Wang, H. Arellano-Santoyo, P.A. Combs, J.W. Shaevitz, P Natl Acad Sci USA, 107 (2010) 9182-9185.
[5] A. Typas, M. Banzhaf, C.A. Gross, W. Vollmer, Nat Rev Microbiol, 10 (2012) 123-136.

[6] G.H. Lan, C.W. Wolgemuth, S.X. Sun, P Natl Acad Sci USA, 104 (2007) 16110-16115.
[7] M.T. Cabeen, G. Charbon, W. Vollmer, P. Born, N. Ausmees, D.B. Weibel, C. Jacobs-Wagner, Embo J, 28 (2009) 1208-1219.
[8] F.W. Si, B. Li, W. Margolin, S.X. Sun, Sci Rep-Uk, 5 (2015).
[9] A. Amir, F. Babaeipour, D.B. McIntosh, D.R. Nelson, S. Jun, P Natl Acad Sci USA, 111 (2014) 5778-5783.
[10] Y. Deng, M.Z. Sun, J.W. Shaevitz, Phys Rev Lett, 107 (2011).
[11] X. Yao, M. Jericho, D. Pink, T. Beveridge, J Bacteriol, 181 (1999) 6865-6875.
[12] N.I. Abu-Lail, T.A. Camesano, Colloids Surf B Biointerfaces, 51 (2006) 62-70.
[13] A. Cerf, J.C. Cau, C. Vieu, E. Dague, Langmuir, 25 (2009) 5731-5736.
[14] Y.Y. Chen, C.C. Wu, J.L. Hsu, H.L. Peng, H.Y. Chang, T.R. Yew, Langmuir : the ACS journal of surfaces and colloids, 25 (2009) 4607-4614.
[15] P. Eaton, J.C. Fernandes, E. Pereira, M.E. Pintado, F.X. Malcata, Ultramicroscopy, 108 (2008) 1128-1134.
[16] C.C. Perry, M. Weatherly, T. Beale, A. Randriamahefa, J Sci Food Agr, 89 (2009) 958-964.
[17] G.K. Auer, T.K. Lee, M. Rajendram, S. Cesar, A. Miguel, K.C. Huang, D.B. Weibel, Cell Syst, 2 (2016) 402-411.
[18] Y. Caspi, Plos One, 9 (2014).
[19] H.H. Tuson, G.K. Auer, L.D. Renner, M. Hasebe, C. Tropini, M. Salick, W.C. Crone, A. Gopinathan, K.C. Huang, D.B. Weibel, Mol Microbiol, 84 (2012) 874-891.
[20] A. Boulbitch, B. Quinn, D. Pink, Phys Rev Lett, 85 (2000) 5246-5249.
[21] J.C. Gumbart, M. Beeby, G.J. Jensen, B. Roux, Plos Comput Biol, 10 (2014).
[22] X. Sun, W.D. Weinlandt, H. Patel, M. Wu, C.J. Hernandez, Lab Chip, 14 (2014) 2491-2498.
[23] A. Lenshof, T. Laurell, Microscale Acoustofluidics, (2015).
[24] A.G. Santiago, T.Y. Chen, L.A. Genova, W. Jung, A.M. George Thompson, M.M. McEvoy, P. Chen, P Natl Acad Sci USA, 114 (2017) 6694-6699.
[25] A. Srivastava, in: Theoretical & Appl Mechanics, Cornell, Ithaca, 2016.
[26] S. Timoshenko, S. Woinowsky-Krieger, Theory of plates and shells, 2d ed., McGraw-Hill, New York,, 1959.
[27] L. Furchtgott, N.S. Wingreen, K.C. Huang, Mol Microbiol, 81 (2011) 340-353.
[28] T.Y. Chen, A.G. Santiago, W. Jung, L. Krzeminski, F. Yang, D.J. Martell, J.D. Helmann, P. Chen, Nat Commun, 6 (2015).
[29] D.S. Cayley, H.J. Guttman, M.T. Record, Biophys J, 78 (2000) 1748-1764.
[30] A.L. Koch, Res Microbiol, 141 (1990) 119-130.

Chapter 2. Estimation of Cell Envelope Young's Modulus

2.1 Introduction

The bacterial cell wall plays a pivotal role in survival of bacteria. It helps maintain cell shape during cell growth and cell division. Most importantly, it is believed to be the dominant stress-bearing component in bacteria [1]. Bacterial mechanical properties have been examined through the use of atomic force microscopy, optical trapping, fluidic bending, or agarose gel encapsulation. The reported Young's moduli from these techniques span over two orders of magnitude (Table 1.1). The extrusion loading microfluidic device (see section 1.1.3) has been shown capable of assessing the bacteria stiffness qualitatively [2]: at a given applied pressure, less stiff cells traveled further into traps than stiff cells. The distance traversed by cells in traps hence serves as an indicator of bacteria stiffness. This technique is able to distinguish two strains of bacteria that feature different peptidoglycan thickness and thus cell wall stiffness.

Our research goal is to quantitatively determine Young's modulus of the cell envelope of *Escherichia coli*, using the data from experiments involving stepwise increases in the magnitude of extrusion loading (see section 1.2.1). We used both analytical and finite element models.

2.2 Analytical Model

2.2.1 Methods

Here we use the analytical model developed by Srivastava [3], which was derived from a force balance using transversely isotropic constitutive laws and measures of cell dimensions at two or three different load magnitudes (see section 1.2.2). The closed form solution for cell envelope Young's modulus can be obtained as follows: first, consider longitudinal force balance on the upstream and the downstream end cap in configuration 1 and 2. Solving these balance equations and substituting the constitutive law, Equation (1.6), we have an expression for change in turgor pressure in the cell as,

$$P_{t2} - P_{t1} = \frac{(P_{u2}r_2 - P_{u1}r_1) + (P_{d2}r_2 - P_{d1}r_1)}{2} + \frac{2tE_h}{\gamma - {\upsilon_{ha}}^2}\left(\frac{l_2 - l_1}{l_1} + \upsilon_{ha}\frac{r_2 - r_1}{r_1}\right) \tag{2.1}$$

Recall that we have already obtained an expression for change in turgor pressure solved from hoop force balance (see section 1.2.2), Equation (1.14). Combining Equation (2.1) and Equation (1.14) and rearranging the terms yield:

$$\begin{aligned}\frac{{r_1}^2(\Delta P_2 - \Delta P_1)}{2l_1(f+\alpha)} = {} & \frac{r_1(P_{u2} - P_{u1} + P_{d2} - P_{d1})}{2} \\ & + \frac{tE_h}{\gamma - {\upsilon_{ha}}^2}\left[(2 - \upsilon_{ha})\frac{l_2 - l_1}{l_1} + (2\upsilon_{ha} - \gamma)\frac{r_2 - r_1}{r_1}\right]\end{aligned} \tag{2.2}$$

In the stepwise increases in extrusion loading experiments, we had three loading configurations. Thus we can treat configuration 1 as the reference state and configuration 3 as another deformed state in addition to configuration 2, and write a similar equation:

$$\frac{{r_1}^2(\Delta P_3 - \Delta P_1)}{2l_1(f+\alpha)} = \frac{r_1(P_{u3} - P_{u1} + P_{d3} - P_{d1})}{2} + \frac{tE_h}{\gamma - {\upsilon_{ha}}^2}\left[(2-\upsilon_{ha})\frac{l_3 - l_1}{l_1} + (2\upsilon_{ha} - \gamma)\frac{r_3 - r_1}{r_1}\right] \tag{2.3}$$

Dividing Equation (2.3) by Equation (2.2), we obtain an equation expressing the cell wall Young's modulus in the hoop direction as:

$$\frac{2tE_h}{\gamma - {\upsilon_{ha}}^2} = \frac{(\Delta P_2 - \Delta P_1)(P_{u3} - P_{u1} + P_{d3} - P_{d1})r_1 - (\Delta P_3 - \Delta P_1)(P_{u2} - P_{u1} + P_{d2} - P_{d1})r_1}{(\Delta P_3 - \Delta P_1)\left[(2-\upsilon_{ha})\frac{l_2 - l_1}{l_1} + (2\upsilon_{ha} - \gamma)\frac{r_2 - r_1}{r_1}\right] - (\Delta P_2 - \Delta P_1)\left[(2-\upsilon_{ha})\frac{l_3 - l_1}{l_1} + (2\upsilon_{ha} - \gamma)\frac{r_3 - r_1}{r_1}\right]} \tag{2.4}$$

2.2.2 Results

Applying experimental data (Figure 1.2) to Equation (2.4) makes it possible to calculate cell envelope Young's modulus. Experimental parameter values included measures of applied pressures and cellular dimensions in three loading configurations. Additionally, we used 4 nm as the cell envelope thickness [4, 5], a Poisson's ratio in the hoop-axial direction of 0.34 [6] and the anisotropy coefficient of 2.0 [4, 7]. The resulting Young's moduli in the hoop direction calculated from Equation (2.4) were distributed in a range of -495 – 3524 Pa (the red circles in Figure 2.1) with an average value of 155 Pa. The results were not sensitive to the variation in cell wall thickness, Poisson's ratio, or anisotropic coefficient within the reported ranges. Note that the literature indicates cell envelope Young's modulus is commonly on the order of MPa (Table 1.1).

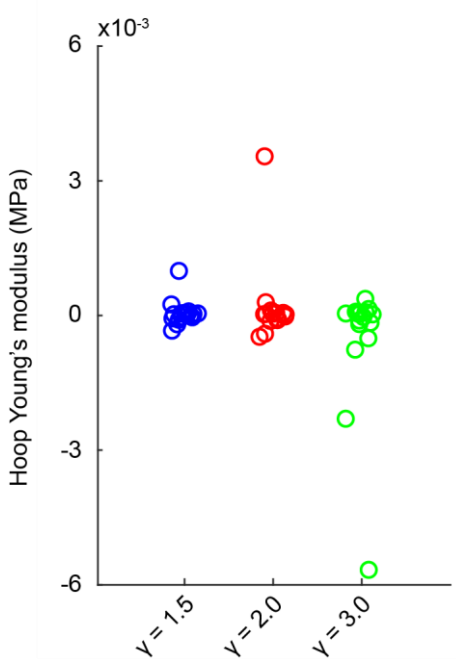

Figure 2.1 Hoop Young's modulus calculated from the analytical model. Equation (2.4) input with the experimental data (n = 17) and reported parameters determines the cell envelope Young's modulus in the hoop direction. Three anisotropic coefficients are tested.

The Coulomb friction coefficient can be estimated by solving Equation (2.2) and (2.3) together. The resulting friction coefficients were distributed in a range of 0.037 – 0.105 with an average value of 0.078.

2.2.3 Discussion

The cell envelope Young's modulus determined with the analytical model (~100 Pa) was over five orders of magnitude smaller than the reported values (~10 MPa). The closed form solution for Young's modulus, in particular Equation (2.4) is shown to be sensitive to the measurements on the dimensions of trapped cells (Figure 2.2). By rewriting Equation (2.4) in a linear form that involves parameterizing any two dimensions from deformed configurations, for

example, cell lengths l_2* and l_3* ('*' signs here denote that the dimensions are now variables instead of measured values), we have

$$l_3{}^* = \frac{\Delta P_3 - \Delta P_1}{\Delta P_2 - \Delta P_1} l_2{}^* + \frac{\Delta P_3 - \Delta P_1}{\Delta P_2 - \Delta P_1}\left(\frac{2\upsilon_{ha} - \gamma}{2 - \upsilon_{ha}}\frac{r_2 - r_1}{r_1} - 1\right) l_1 - \left(\frac{2\upsilon_{ha} - \gamma}{2 - \upsilon_{ha}}\frac{r_3 - r_1}{r_1} - 1\right) l_1 - \frac{A}{\Delta P_2 - \Delta P_1}\frac{\gamma - \upsilon_{ha}{}^2}{2 - \upsilon_{ha}}\frac{l_1}{2tE_h} \quad (2.5)$$

, where $A = (\Delta P_2 - \Delta P_1)(P_{u3} - P_{u1} + P_{d3} - P_{d1})r_1 - (\Delta P_3 - \Delta P_1)(P_{u2} - P_{u1} + P_{d2} - P_{d1})r_1$.

Equation (2.5) indicates that when the dimension measurements varied by 25% (due to experimental errors, resolution limits, etc.), the obtained Young's moduli changes by as much as six orders of magnitude (Figure 2.2F). Similar methods can be applied to any other two parameterized dimensions (r_2*, r_3*, l_2*, l_3*) and show the same result. Therefore, precise determination of Young's modulus using the analytical requires accuracy of experimental measurements well beyond the capacity of the microscopes currently being used.

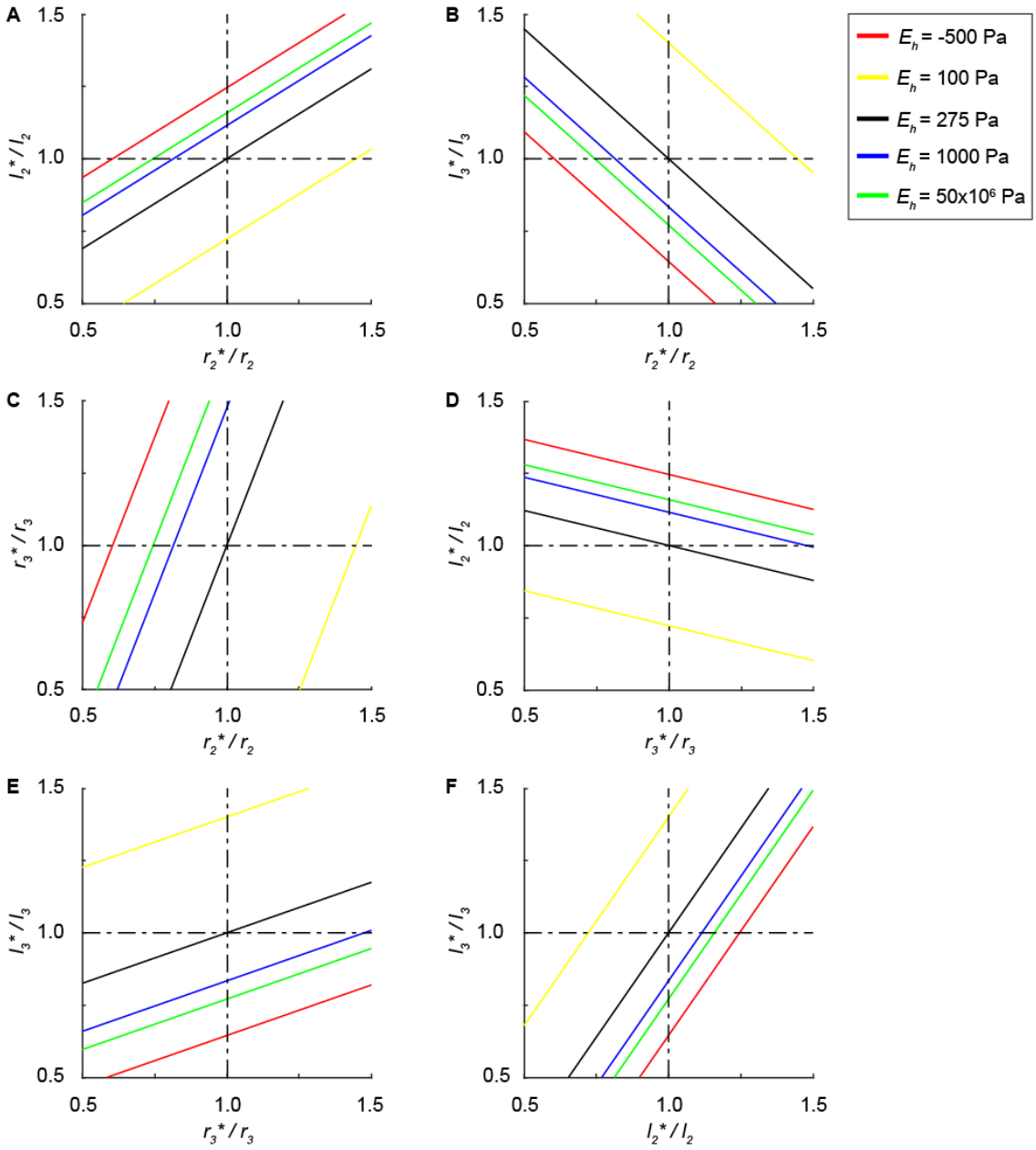

Figure 2.2 Closed form solution for determination of hoop Young's modulus shows sensitivity to experimental measurements. An example of Equation (2.4) rewritten in linear forms. The black solid line in each plot denotes a linearized Equation (2.4) assigned with hoop Young's modulus solved by Equation (2.4) (Figure 2.1).

There are a few limitations to the analytical model that we must consider. First, the model is based on small strain assumption. The experimental results showed that the average axial strain

is 0.14 between configuration 1 and 2, and 0.41 between configuration 1 and 3 (Figure 1.2C). The average hoop strain is -0.12 between configuration 1 and 2, and -0.26 between configuration 1 and 3 (Figure 1.2B). Hence, the magnitude of the deformations exceeded where small strain condition applies.

In addition, the analytical model assumes no material flow between trunk and end caps of a trapped cell. The lengthening of a cell during extrusion loading in the analytical model is a result of extension in the cell trunk. However, finite element modeling (see section 1.3.2) suggests that as a cell traveled further downstream in response to an increase in applied extrusion loading, a portion of end caps (~20% of the cap length when ΔP is 15 kPa, ~27% of the cap length when ΔP is 24 kPa) was bent to channel walls and became part of trunk, leading to lengthening of the cell. This mode of deformations was not characterized by the analytical model.

For these reasons, we concluded that the analytical model, while reasonable, was not able to describe the experimental results and a finite element model was developed.

2.3 Finite Element Model

2.3.1 Methods

We created a finite element model of the bacteria submitted to extrusion loading using Abaqus (CAE 6.9-EF2, Dassault Systems, Providence, RI). A bacterium within the extrusion loading system was modeled as axisymmetric. The cell envelope was modeled as an isotropic

material with Young's modulus E and Poisson's ratio υ using solid elements. The finite element model consisted of 2,880 four-node bilinear quadrilateral elements (4 elements across the cell thickness, CAX4R elements). The thickness of the cell envelope t was chosen as 6 nm [4]. Channel walls were represented by rigid surfaces with dimensions determined from the microfluidic device (see section 1.1.3). Contact between the cell envelope and the channel walls was simulated using a surface-to-surface contact. Coulomb friction was applied between the cell envelope and channel walls with an estimated friction coefficient $f = 0.04$ (see section 2.2.2). Geometric nonlinearities were included in the finite element model.

A stepwise increase in extrusion loading (increase in ΔP) was modeled by applying the difference in boundary conditions (fluidic pressures and cell dimensions) between two loading configurations to a cell envelope in the reference configuration (Figure 2.3). In particular, the difference in applied pressures between the reference and the deformed configuration, $P_{u2} - P_{u1}$ and $P_{d2} - P_{d1}$ (or $P_{u3} - P_{u1}$ and $P_{d3} - P_{d1}$) was applied on the caps in the form of pressure. The difference in trunk radius, $R_2 - R_1$ (or $R_3 - R_1$) was applied by moving the channel walls. In addition, an internal pressure, δP_t was applied to the inner surface of the cell envelope, characteristic of the increase in turgor pressure as a cell undergoes an increase in extrusion loading (see section 1.2.3). The magnitude of the change in turgor pressure was estimated from Equation (2.1). A pin at the mid cell was included to inhibit rigid body motion of the cell

envelope in channel walls.

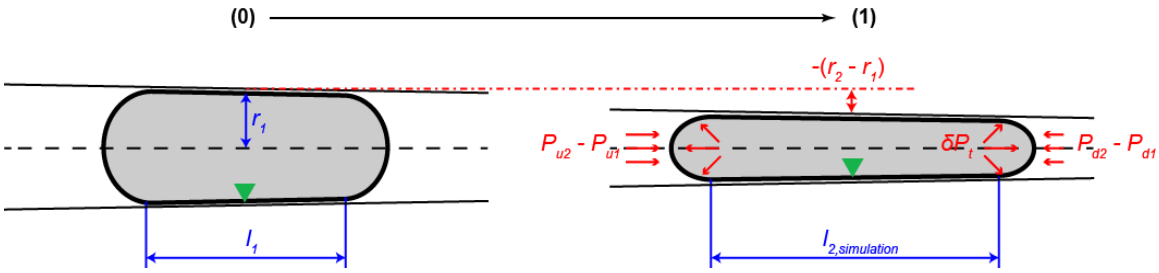

Figure 2.3 Finite element method for determination of the cell envelope Young's modulus. The cell on the left represents the reference configuration (configuration 1). The cell on the right is the deformed configuration (configuration 2 or 3) obtained from a simulation. Numbers mark the steps in a simulation. The green triangles represent the pins that inhibit longitudinal displacement.

A parametric analysis was performed to iteratively determine the cell envelope Young's modulus (Table 2.1). An array of isotropic Young's moduli was assigned to the finite element model. If the observed cell length matches experimental results we record the cell envelope Young's modulus. Poisson's ratio is yet to be examined in the literature and may also affect the simulation cell length; thus it was parameterized in a range from 0.0 to 0.5. The parametric analysis method can be expressed as follows:

$$(E, \upsilon) \xrightarrow{\text{FE model}} l_{2,simulation} \overset{\text{Compare}}{\Longleftrightarrow} l_{2,experiment} \tag{2.6}$$

Table 2.1 Ranges of tested parameters for the cell envelope in the finite element model. A total of 517 simulations are performed for each cell in the parametric analysis.

Parameter	Definition	Parameter Range	Reported Range
E	Isotropic Young's Modulus	10 – 240 MPa	2 – 220 MPa (Table 1.1)
υ	Poisson's Ratio	0.0 – 0.5	–

2.3.2 Results

The parametric finite element simulations yielded cell lengths obtained at different Young's moduli (Figure 2.4). The simulation cell lengths are consistently larger than the cell length obtained experimentally by at least 20%. The simulation cell length decreases as expected when the cell envelope Young's modulus increases, but after Young's modulus exceeds 30 MPa the cell length plateaus. The cell lengths drop by 7% when Poisson's ratio is decreased from 0.5 to 0.0.

Increasing the friction coefficient by 10 times resulted in only a reduction in simulation cell length by 4%.

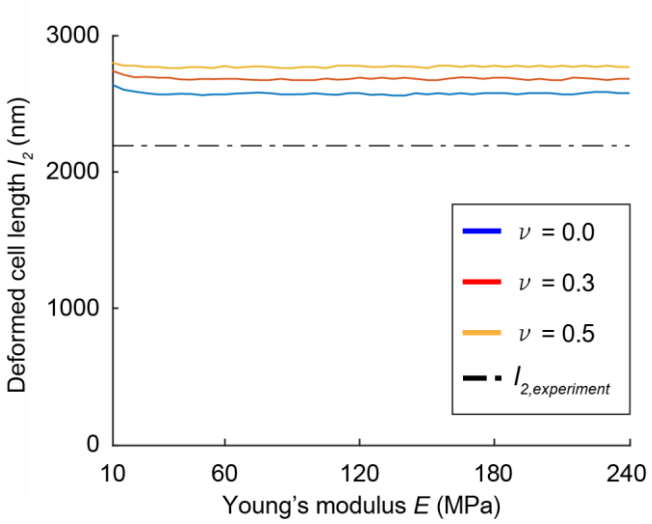

Figure 2.4 Results of the parametric finite element analysis on the cell envelope Young's modulus. One example of the relations between the isotropic Young's modulus and the resulting cell length. The dashed line represents the cell length obtained experimentally at the deformed configuration.

2.3.3 Discussion

In our simulations, the cell length was not sensitive to the change in the cell envelope Young's modulus. Deformation is generally reduced in a stiff material than in a less stiff material when the applied loads remain identical. The finite element simulation in theory yields greater resulting cell length as the assigned Young's modulus is small, generating a monotonically decreasing trend of simulation cell length as the Young's modulus increases. The parametric analysis is based on this concept and iteratively determines Young's modulus that dictates deformation similar to the experimental results. However, the simulation results indicated that the resulting cell length remained unchanged across the tested range of Young's moduli (Figure 2.4), preventing any conclusions regarding Young's modulus in these simulations.

There are a number of reasons why the simulation results did not match the experimental results, one of which is that the simulation cell length was consistently greater than the experimental value. The overestimated cell length may be partially explained by the curvature of the end caps. As previously shown, the lengthening of a cell submitted to extrusion loading involves part of end caps bent to channel walls. This suggests that as the radius of end caps increases (curvature decreases), the proportion of end caps that would be bent to channel walls decreases. Additional simulations in which the curvature of end caps was decreased by 22% (from hemispherical to relatively flat caps) resulted in a reduction in simulation cell lengths by

14%. Although in theory we could parameterize the curvature of end caps in the parametric analysis, the insensitivity of cell length to Young's modulus may produce multiple Young's moduli that dictate deformations equal to the experimental results.

The use of a pin was to inhibit rigid body motion, but meanwhile it altered the deformation mode. With the presence of a pin, the upstream half of a cell was subjected to frictional force pointing downstream as the envelope lengthened toward the upstream. In the downstream half, the frictional force pointed to the opposite direction. Axial stress in a cell envelope is a function of frictional force given by the longitudinal force balance on a section of cell envelope. The frictional force that reversed its direction at the pin yielded axial stress and strain distributed in a V shape (Figure 2.5), which denotes that lengthening was greater near the end caps and smaller around the pin. However this is different from the linear pattern we have shown previously (Figure 1.5).

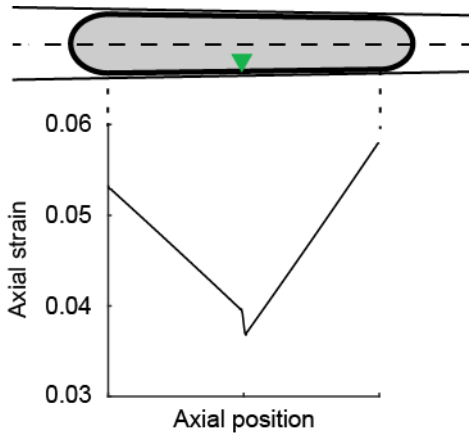

Figure 2.5 Axial strain in a cell from the finite element model developed for Young's modulus determination. The axial strain distribution across the length of trunk, in which E = 50 MPa, υ = 0.3. The green triangle represents the pin that inhibits longitudinal displacement.

2.3.4 Future Work

The major issues with the parametric finite element method are that deformations exhibited insensitivity to the change in Young's modulus and the use of a pin altered the way a cell envelope deformed. In the future finite element model, pressures are the only boundary conditions we apply (current model applied both pressures and deflections) and cells are modeled without a pin. The parametric finite element model generated for stress analysis (see section 1.3.2) has shown that deformations were sensitive to the choice of cell envelope Young's modulus when all the boundary conditions were in the form of pressure. In addition, cells were free to slide in tapered channels in the finite model used for stress analysis and they deformed in a way much similar to what was seen experimentally. Additional details on the future parametric finite element approach for determining cell envelope Young's modulus include: we record resulting trunk radii, instead of cell length, and compare them to the experimental results due to the consistency in cell

width regardless of cell growth and bending of end caps. A cell envelope is modeled as a transversely isotropic material. Moreover, the change in turgor pressure can influence how downstream a cell travels in tapered channel and thus the resulting trunk radius, so the change in turgor pressure is set as a free variable. The procedures of the proposed future analysis can be abbreviated as follows:

$$(E_a, \delta P_t) \xrightarrow{\text{FE model}} r_{2,simulation} \overset{\text{Compare}}{\Longleftrightarrow} r_{2,experiment} \tag{2.7}$$

, where E_a is the envelope Young's modulus in the axial direction and δP_t is the change in turgor pressure between two loading configurations.

For each cell, ranges of Young's moduli and the change in turgor pressures are obtained. Examinations on all cells (n = 17) and the two deformed configurations (configuration 2 and 3) enable us to probe the average Young's modulus of the cell envelope.

2.4 Reference

[1] D.M. Morris, G.J. Jensen, Annu Rev Biochem, 77 (2008) 583-613.
[2] X. Sun, W.D. Weinlandt, H. Patel, M. Wu, C.J. Hernandez, Lab Chip, 14 (2014) 2491-2498.
[3] A. Srivastava, in: Theoretical & Appl Mechanics, Cornell, Ithaca, 2016.
[4] X. Yao, M. Jericho, D. Pink, T. Beveridge, J Bacteriol, 181 (1999) 6865-6875.
[5] L. Gan, S.Y. Chen, G.J. Jensen, P Natl Acad Sci USA, 105 (2008) 18953-18957.
[6] J.C. Gumbart, M. Beeby, G.J. Jensen, B. Roux, Plos Comput Biol, 10 (2014).
[7] Y. Deng, M.Z. Sun, J.W. Shaevitz, Phys Rev Lett, 107 (2011).